Stronger Aramids through Molecular Design and Nanoprocessing

A. Rapakousiou, A. López-Moreno, B. Nieto-Ortega, M. M. Bernal, M. A. Monclús, S. Casado, C. Navío, L. R. González, J. P. Fernández-Blázquez, J. J. Vilatela and E. M. Pérez

Stronger Aramids through Molecular Design and Nanoprocessing

Amalia Rapakousiou,[a] Alejandro López-Moreno,[a] Belén Nieto-Ortega,[a] M. Mar Bernal,[a] Miguel A. Monclús,[b] Santiago Casado,[a] Cristina Navío,[a] Luisa R. González,[c] Juan P. Fernández-Blázquez,[b] Juan J. Vilatela,[*,b] and Emilio M. Pérez[*,a]

We introduce oligo-(1,6-pyrene terephthalamide, oPyrTA) as an oligoamide model for Kevlar®. Through comparison with an oligo-(*p*-phenylene terephthalamide, oPTA) of similar molecular weight, this work shows that the incorporation of polycyclic aromatic pyrene moieties improves drastically the mechanical properties of the structure, increasing elastic nanoindentation-determined modulus and hardness by factors of 1.9 and 4.3, respectively. Liquid deprotonated dispersions of oPyrTA nanofibers were used as nanoscale building block for producing large-surface, free-standing oligomer macroscopic nanofilms. This 2D assembly leads to further significant improvements in reduced modulus and hardness (more than twice) compared to the starting oligomer macroscale fibres, due to a better re-organizational arrangement of the oPyrTA nanofibers in the nanofilms, formed under 2D spatial confinement.

Introduction

Ultra-strong high performance materials have been extensively explored for advanced technological applications and everyday life. In this context, aromatic polyamides (aramids) are considered as super-engineering polymers due to their high tensile strength and high chemical/thermal stability.[1-5] Their high-performance properties result from their rigid structure with *para*-substituted aromatics, and from the amide groups that create a linear structure with high cohesive energy and crystallization tendency due to the intermolecular hydrogen bonds (H-bonds).[3, 6] Most notably, the commercial poly(*p*-phenylene terephthalamide) (**oPTA**), also known as Kevlar®, is a well-known *para*-aramid synthetic macroscale fiber which is widely used in a variety of applications, including bulletproof vests and protective clothes, as well as aircraft, watercraft and automotive industries.[7-14] **oPTA** interchains' noncovalent bonds make this oligomeric material extremely strong and stiff with a tensile strength of 3.6 GPa and modulus of around 124 GPa.[15] However, the processing of polyaramides is very challenging because they are completely insoluble in most common solvents (usually they are only soluble in concentrated sulfuric acid) and their melting points are above their decomposition temperature.[16] Another drawback is that the ultraviolet component of sunlight degrades and decomposes Kevlar, a problem known as UV degradation.[17] Therefore, researchers' attention has turned towards small modifications in the main chain of aramids, i.e. the use of polycyclic aromatic hydrocarbons as polymeric units[18, 19] enhances the solubility and processability of these materials, facilitating their study. Another interesting approach based on Takayanagi´s work[20] was the deprotonation of aromatic polyamides. Subsequent addition of proton donors to the polyanionic polymers enhanced the rate of polymer dissolution and gave higher solubilities and lower solution viscosities. This concept opened the way to their use in composite materials.[21, 22] Consequently, the pioneering work of Kotov's group[23] providing liquid dispersions of aramid nanofibers by controlled dissolution of the corresponding macroscale fibres rendered for the first time aramids accessible as a nanoscale building block, useful for the functional design of nanocomposites.[24-27]

Here, we present a novel aramid featuring 1,6-pyrene diamine as building block: 'poly(1,6-pyrene terephthalamide)' (**oPyrTA**). The incorporation of flat aromatic pyrene units results in reinforced H-bonds and π-stacking, promising enhanced mechanical properties. Interestingly, **oPyrTA** spontaneously assembles into flattened fibres. Building on this natural tendency, we produce large-surface, mechanically strong, free-standing, oligomer-nanofilms of **oPyrTA** aramids made from dissoluted **oPyrTA** nanofibers as the only building block.

Results and discussion

Both **oPyrTA** and **oPTA** oligomers were prepared by a polycondensation reaction between commercial terepthaloyl chloride and 1,6-diaminopyrene or *p*-phenylenediamine, respectively, in a NMP solution containing $CaCl_2$ (Fig. 1). In both cases, the formation of a polymeric material was observed

in less than 30 minutes (Supporting Information, p.p. S3). The filtered material formed a powder, which was further analyzed.

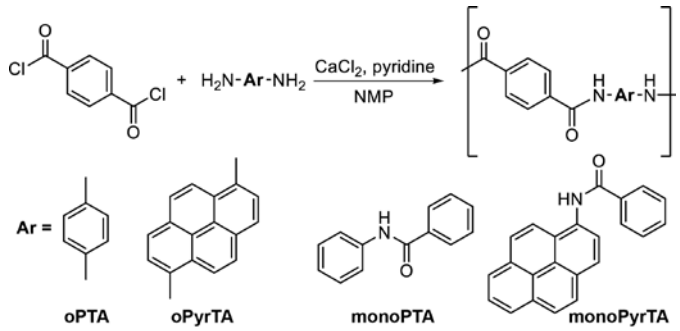

Figure 1. Synthesis and chemical structures of oligomers **oPTA** and **oPyrTA** and of model monomers **monoPTA** and **monoPyrTA**. See the Supporting Information for experimental details.

The FT-IR spectra of **oPTA** and **oPyrTA** are shown in Figure 2a. Both display an absorption band at around 3250-3350 cm^{-1} due to the characteristic N-H stretching mode of secondary amides. Stretching vibrations of C=O are apparent at around 1640 cm^{-1} while at 1500-1550 cm^{-1} and 1200-1300 cm^{-1} the absorption bands due to deformation of N-H and C-N stretching coupled modes can be observed. Interestingly, a broad shoulder in the N-H stretching mode appears in both oligomers, that allows us to distinguish the intra (sharper peak) and inter (broad shoulder) fibrous H-bonding of the macroscale materials. For **oPyrTA** C=O and N-H stretching bands appear at lower wavenumbers compared to **oPTA** (i.e. N-H stretching of **oPyrTA** appears at a considerable lower wavenumber, that of 80 cm^{-1}). Comparison of both oligomers with their monomeric analogues, the newly synthesized *N*-pyrenylbenzamide (**monoPyrTA**) (Supporting Information, p.p S3) and commercially available benzanilide (**monoPTA**), respectively, confirms the same tendency (Figure 2, insets), indicating stronger H-bonding in **oPyrTA** versus **oPTA** and in oligomers versus their monomeric analogues.

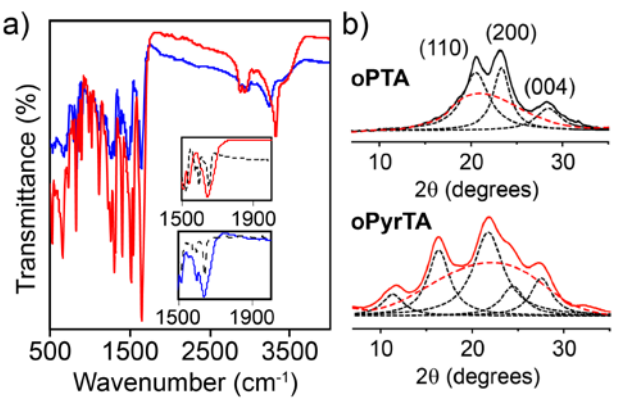

Figure 2. a) FT-IR spectra of **oPTA** (red) and **oPyrTA** (blue). Insets: comparison of both oligomers with their monomeric analogues: **monoPTA** and **monoPyrTA (black)**. b) XRD patterns of oPTA and oPyrTA.

UV−Vis spectroscopy of **oPyrTA** showed a strong absorption band peaking at λ = 383 nm, tentatively assigned to π → π* transitions, which is red shifted with respect to **oPTA** (λ = 340 nm), suggesting that it should possibly be more resistant to ultraviolet light exposure (Figure S2).[28]

The crystalline structures of **oPTA** and **oPyrTA** were investigated and compared by XRD (Figure 2b). The sharper diffraction peaks of **oPTA** were observed at Bragg angles of 20.59°, 23.16° and 28.28° which can be assigned to (110), (200) and (004), respectively, reflections of a monoclinic (pseudo-orthorhombic) unit cell.[23, 29] **oPyrTA** displays a different diffraction pattern, showing five diffraction peaks at 11.70°, 16.33°, 21.70°, 24.30° and 27.40°, as **oPyrTA** crystallizes in a different unit cell. The bigger size of pyrene causes a distortion of the pseudo-orthorhombic unit cell, which has a γ angle of approximately 90°, probably by reducing this γ angle and then crystallizing into a monoclinic unit cell. The crystallinity percentage of **oPTA** and **oPyrTA** was estimated subtracting Compton backgrounds and taking the percentage of crystalline peak areas over the amorphous area. **oPyrTA** presents a crystallinity of 25% whereas **oPTA** a crystallinity of 35%, which is consistent with previous reports on **oPTA** oligomers.[29] **oPTA** also presents sharper peaks, which is associated with longer crystal sizes and stronger ability to crystallize.

The thermal stability of the aramids **oPTA** and **oPyrTA** was evaluated by thermogravimetric analysis (TGA, N_2, 10°C min^{-1}). As shown in Figure S3 both **oPTA** and **oPyrTA** begin to decompose at 495 °C (5% weight loss), whereas their 50% weight decomposition temperature stands at around 590°C and 560 °C, respectively. Therefore, both aramids exhibit high thermal stability within the same range (<6% difference) as typically reported Kevlar-like polymers.[30, 31]

The intermolecular interactions of the aggregates formed by **oPTA** and **oPyrTA**[32] were studied by performing density functional theory (DFT) calculations at the B97D/6-31G** level[33] (for full computational details see Supporting Information, p.p. S6). As a model of the final structure we built stack layers of the respective monomers, where all the possible interactions were considered. In the case of **oPTA**, the amide groups define an H-bonding network with N-H···O distances of 2.025 Å,[33] whereas, this distance decreases to 1.98 Å for **oPyrTA** (Figure 3). These theoretical data, suggesting stronger H-bonding in **oPyrTA**, are in good agreement with the IR spectra of Figure 2a. Another interesting feature is the distance between the aromatic moieties: 4.25 Å for **oPTA** and 3.84 Å for **oPyrTA**, revealing markedly stronger intermolecular aromatic π-π stacking interactions in the new oligomer, as expected (Figure 3 and Figure S5). The closer π–π distances are probably the main reason behind the shorter H-bond contacts. The enhanced noncovalent interactions in the pyrene analogue are reflected in a significant increase of the total stabilization energy up to 6.06 Kcal mol^{-1} (calculated at −28.60 kcal mol^{-1} for **oPTA** and −34.66 kcal mol^{-1} per monomer for **oPyrTA**).

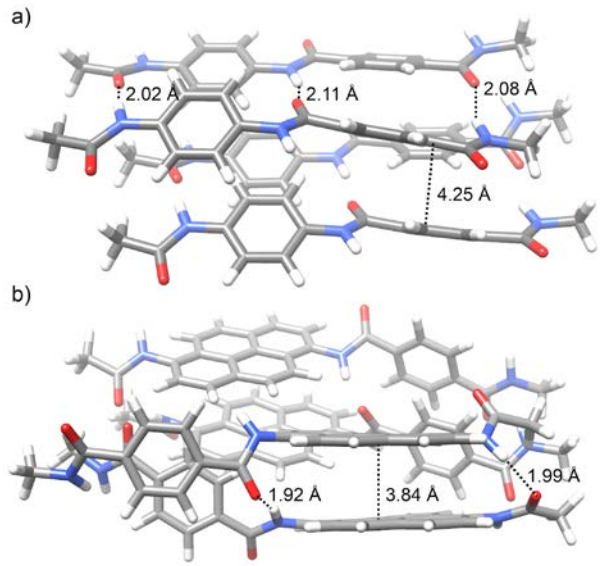

Figure 3. DFT optimized geometries for a) **oPTA** and b) **oPyrTA** tetramers. Representative H-bond and π-π interactions distances are indicated.

With the chemical identity of the aramid oligomers **oPTA** and **oPyrTA** confirmed, we proceeded to estimate their molecular weight. Due to complete insolubility in most common solvents, except conc. H_2SO_4, we resorted to a combination of different techniques which showed good consistency: Viscosity measurements (Oswald method) and UV−Vis spectroscopy (using Lambert-Beer law) giving an average molecular weight of $3 \times 10^3 \pm 500$ Da for oligomer **oPTA** and $5 \times 10^3 \pm 1000$ Da for oligomer **oPyrTA**, corresponding to 12 ± 2 and 13 ± 3 monomer units (Table S1-S2, measurement details in Supporting Information, p.p S8-S9).

We consistently observed that the powder sample of **oPyrTA** was made up of fibres. The morphology of the **oPyrTA** macroscopic fibres was investigated through scanning electron microscopy (SEM). Figure 4a shows SEM images of the **oPyrTA** powder, directly deposited onto a SEM sample holder. Very long fibres, hundreds of µm and up to the mm scale, are clearly visible (white circle), together with smaller fragments. A closer look reveals that the fibres are flattened (Figure 4a, inset): we attribute this flattening to the increased anisotropy introduced by the pyrene unit. Kevlar macroscale threads and fibres are found to split into nanoscale ones, by reaction with KOH in DMSO through abstraction of the mobile H-bonds from the –NH amide groups, therefore reducing the strength of interfibrous hydrogen bonding while at the same time producing electrostatic repulsion.[23] Based on this concept, we proceeded to study the dissolution of **oPyrTA** under strongly basic conditions. Stirring for 3 days the solid **oPyrTA** in a KOH/DMSO (c = 0.18 M) solution, gave a dark-orange solution (Figure S14) of deprotonated **oPyrTA** nanofibers (Supporting Information, p.p. S14). The solubility is due to dissociation of the weaker interfibrous H-bonds which is partly generating negatively charged N anions stabilized by the potassium cations. This is manifested by the FT-IR spectrum of the orange solution showing a big upshift of C=O and N-H peaks (Figure 5a). SEM analysis of the deprotonated sample showed that it consists of **oPyrTA** nanofibers with a 110 ± 10 nm diameter, as a result of the weakening of interfibrous H-bonds and the increase of charge-repulsion between the constitutive nanofibers (Figure 4b and S15 in Supporting Information). AFM analysis showed a height of 1.5 ± 0.3 nm for the produced **oPyrTA** nanofibers (Figure 5b).

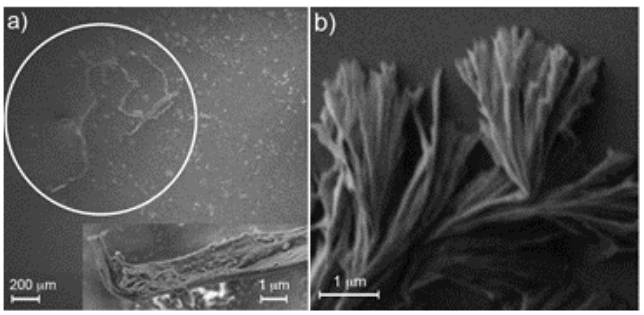

Figure 4. SEM micrographs of **oPyrTA**. a) Low magnification, with white circle around long fibres in the mm range (inset: High magnification detail of the tip of the longest fibre, showing its flattened microstructure b) **oPyrTA** nanofibers.

Taking into account the natural tendency of **oPyrTA** to form flattened fibres,[34] we decided to investigate the formation of nanofilms[35, 36] starting from the nanofibers' solutions, under spatial confinement. To investigate this, 0.05 mL of **oPyrTA** nanofibers solution was deposited on a glass substrate (26 x 76 mm) which had a paper-spacer in both edges (thickness: 180 µm) and subsequently sandwiched with another glass substrate (Figure S16). This system was then dipped into water for 3 days allowing **oPyrTA** nanofibers in the confined space to seize protons from water through a slow and controlled H_2O diffusion into DMSO resulting in gradual neutralization of the **oPyrTA** chains. After 3 days, **oPyrTA** nanofilms were formed and observed floating between the glass substrates (Figure 7a). The color changed from dark-orange to light yellow, an evidence of protonation and re-formation of the previously dissociated hydrogen bonding in **oPyrTA** chains. After work-up (Supporting Information, p.p. S15) the salvaged **oPyrTA** nanofilms on the glass substrate were subjected to various spectroscopic and microscopic analyses for characterization.

FT-IR showed the chemical signature of **oPyrTA** nanofilms as all the characteristic aramid peaks were present. Compared to the initial **oPyrTA** oligomer, IR peaks of **oPyrTA** nanofilms now present a decreased intensity and sharpness (Figure S17). In Figure 5a, a clear downshift of C=O and N-H peaks compared to **oPyrTA** nanofibers was observed, an evidence for the effective reformation of strong H-bonding in nanofilms. Whereas the C=O stretching of **oPyrTA** nanofilms is found at a wavenumber almost identical to C=O stretching of **oPyrTA**, the N-H stretching does not show a shoulder but is interestingly situated between the intra and inter fibrous H-bonded **oPyrTA** N-H peaks, indicating that all H-bonds should be equally strong associated with the optimization of the **oPyrTA** chain conformation in the nanofilm.

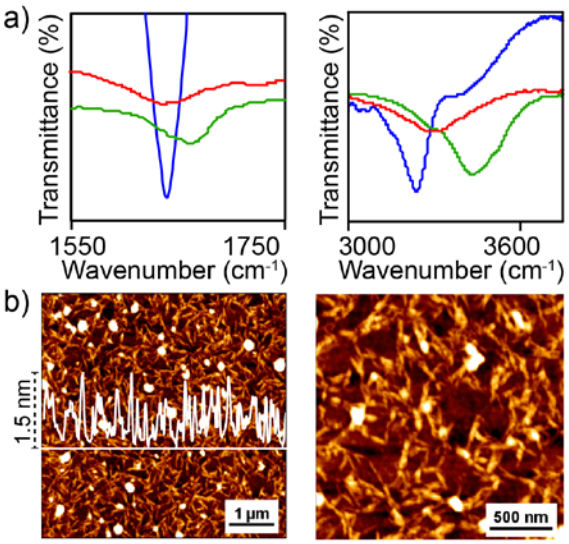

Figure 5. a) Comparative FT-IR spectra of **oPyrTA** (blue), **oPyrTA** nanofibers (green) and **oPyrTA** nanofilms (red) and b) AFM topographic images of **oPyrTA** nanofibers.

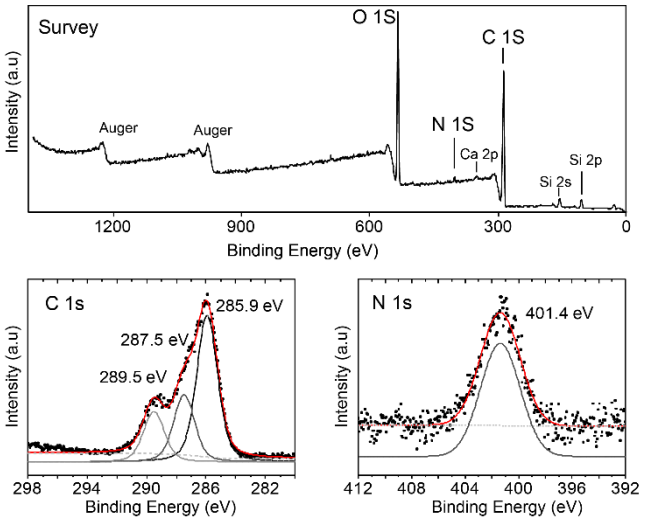

Figure 6. XPS spectroscopy of **oPyrTA** nanofilms: Survey scan (top) and narrow scans on C 1s and on N 1s (bottom).

Raman spectroscopy of the nanofilms shows the characteristic **oPyrTA** aramid peaks which are broader in this case, following the same tendency as FT-IR (Figure S18) whereas TGA analysis revealed two weight losses, one at 390 °C and another at 570 °C highlighting the difference between **oPyrTA** and **oPyrTA** nanofilms. (Figure S19). Finally, the chemical identity of the **oPyrTA** nanosheet material was confirmed by X-ray Photoelectron Spectroscopy (XPS) and Energy Dispersive X-ray Spectroscopy associated with SEM (SEM/EDS mapping). XPS spectra are shown in Figure 6: a survey scan for the whole region detected the presence of the constitutive carbon, oxygen and nitrogen derived from the nanofilms. The core level of SiO2 at 103.5 eV was used for binding energy correction. A narrow scan for N 1s gave a peak centered in 401.4 eV binding energy, characteristic of the amide group, whereas a narrow scan for C 1s showed two main peaks very close to each other: one centered at 289.5 eV and the second broad peak centered at around 286.7 eV. The last were further fitted into three Gaussians-Lorentzians with binding energies of 285.9 eV, 287.5 eV and 289.5 eV corresponding to aromatic Csp^2, C-N and C=O of **oPyrTA** nanofilms. The C/N ratio is calculated as 13/1 (C: 94%, N: 6%) which is in accordance with the actual C/N ratio of nanofilms. Likewise, SEM/EDS mapping indicates that the nanofilm domain contains C and N, whereas it shields the Si signal derived from glass substrate (Figure S20). UV/Vis. of **oPyrTA** nanofilms was also measured showing the characteristic absorption band due to the $\pi \rightarrow \pi^*$ transitions of aromatic C-C bonds, at λ = 385 nm (Figure S21). The appearance of an absorption feature in the red region of the spectra (550-750 nm), characteristic of the formation of pyrene excimers. This band further corroborates the existence of strong pyrene-pyrene interactions in the nanofilms.

The morphology of the nanofilm was then explored by several microscopic techniques. Optical transmission microscopy revealed the nanofilm nature: Figure 7b shows a representative optical microscopic image of **oPyrTA** nanofilm with a domain size exceeding 110 µm, having a folded edge whereas in the inset another fully folded nanosheet can be observed. Figure 7c shows an optical transmission microscopic image of **oPyrTA** nanofilm lying flat on the glass substrate, with a domain size exceeding 180 µm. The area represented by the dotted square was measured by atomic force microscopy (AFM) (Figure 7d) revealing a thickness of 55 nm. The phase image allows to distinguish the nanofilm domain and bare glass substrate (Figure 7e). Another AFM height image of **oPyrTA** nanofilm containing also a folded edge is demonstrated in Figure S22 whose cross-section analysis displays double the thickness (100 nm) of the unfolded nanofilm (50 nm), a further evidence of the tough nature of a nanofilm material. SEM (Figure 7f) shows nanofilms with a flat texture. Observation of the **oPyrTA** nanofilms under low-voltage aberration corrected HRTEM (60 kV, Figure 8) provides a clearer picture of the microstructure of the films. In the low magnification images, we observe that the nanofilm is composed of several thinner layers of oligomer (Figures 8a and b). Within the films, we observe apparently amorphous parts coexisting with relatively large highly crystalline areas (Figure 8c). At this point, it should be remarked that we have probed that crystallization did not appear during the observation under the electron beam. A HRTEM image of the white square on Figure 8 c and its corresponding 2D-FFT are shown in Figure 8d. From these data, we obtain characteristic distances of 0.18 and 0.31 nm. These distances can be tentatively assigned to the shorter and longer intermolecular distances that we observe in the DFT geometry optimization of **oPyrTA** (Figure 3b).

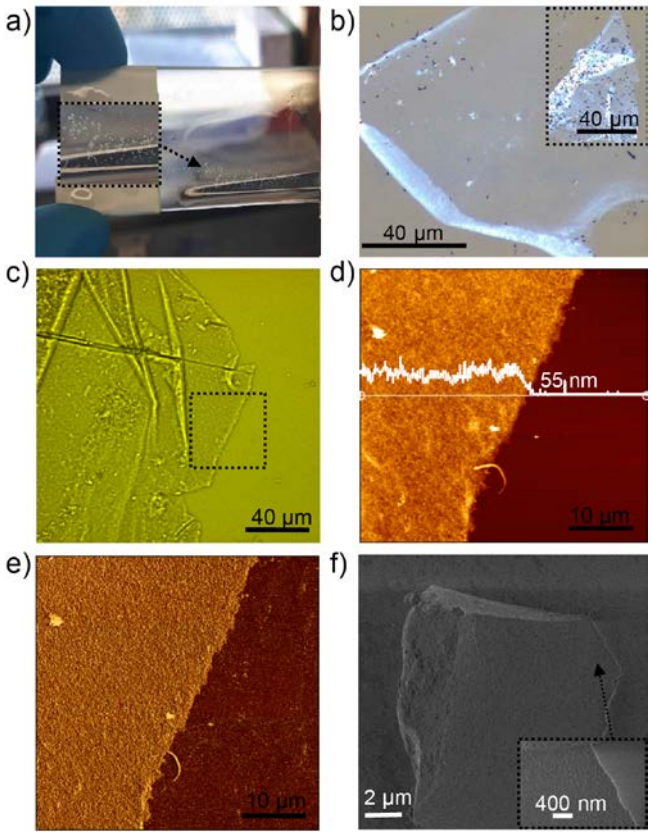

Figure 7. oPyrTA nanofilms: a) Photo before treatment (inset: zoom), b) Optical image (inset: another folded nanofilm), c) Optical image (inset: area measured in AFM), d) AFM topo image, e) AFM phase image and f) SEM image.

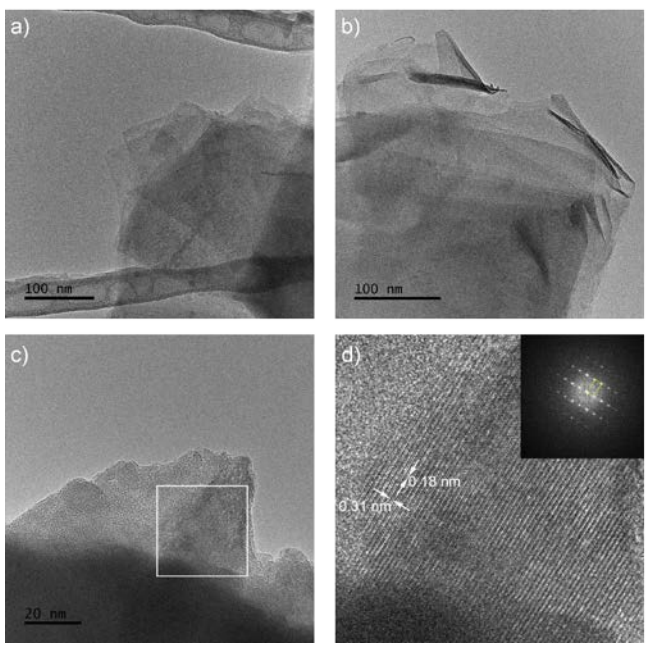

Figure 8. TEM micrographs (60 kV) of **oPyrTA** nanofilms. a-b) Low magnification micrographs showing that each nanofilm is composed of several thinner layers. c) TEM image corresponding to few layers d) HRTEM image performed on the crystalline area marked with a white square in c). Inset shows the 2D-FFT.

The mechanical properties of the powder of **oPyrTA** oligomer were explored by nanoidentation and compared with those of **oPTA**. Over 15 tests were carried out, including indentations on different locations of the sample and the use of different loads and strain rates (Figure S23a). Figure 8a shows representative load-displacement curves obtained on both samples. Following the experimental and mathematical procedure described in the Supporting Information, p.p. S20, elastic reduced modulus and hardness were obtained from the indentation tests. These results are summarized in Table 1. Irrespective of testing conditions, the **oPyrTA** sample was found to be substantially stiffer and stronger than **oPTA**. The superior rigidity of resonance-stabilized pyrene units and the intermolecular stronger π-π stacking between the planar pyrene moieties of **oPyrTA** explain the significantly larger mechanical performance of the oligomer, when compared to **oPTA**.

Upon formation of the nanofilms, this **oPyrTA** shows further improvements in its mechanical properties. Nanoindentation testing of **oPyrTA** nanofilms was carried out on a Hysitron TI950 Triboindenter equipped with either a three-sided pyramidal Berkovich with a tip radius of ~ 350 nm or a cube-corner diamond indenter with a tip radius of < 100 nm. The testing was performed on parts where multiple **oPyrTA** nanofilms were lying flat on the top of each other (therefore larger tested film thickness) in order to minimize the substrate effect. Multiple indentations were performed at different locations of the nanofilm (i.e. see Figure S23b), in load-control mode at different maximum loads, using load-hold-unload cycle times of 30-30-5 s. Finally, all data were analysed with the Oliver and Pharr method.[37] For the evaluation of hardness, plastic deformation is required to occur well within the **oPyrTA** films, which is more easily achieved with a smaller tip radius indenter[38] so the cube-corner tip was used instead. Typical load-displacement curves for Berkovich and cube-corner indentations are shown in Figure 8b, where it can be clearly seen that for similar indentation loads, the cube-corner indenter penetrates much deeper into the **oPyrTA** films, deforming more plastically, as indicated by the larger area within the curves for similar depths. For the cube-corner indentation performed at a maximum force over 100 µN, a change in the slope of the loading curve observed at ≈145 nm indicates that the plastic deformation zone that developed underneath the indenter is reaching the harder substrate.

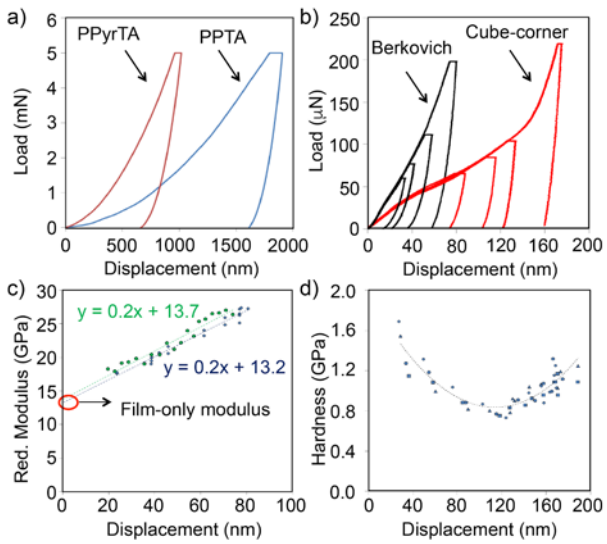

Figure 9. a) Representative oligomeric force-displacement curves obtained on **oPTA** (blue) and oPyrTA (red) samples for a maximum indentation load of 5 mN, (b) Representative load-displacement curves of oPyrTA films from nanoindentation tests performed with Berkovich and cube-corner indenters at different maximum loads, (c) Reduced modulus versus Berkovich indenter penetration depth of oPyrTA films for two different areas showing the extrapolation to zero displacement to obtain the "film-only" modulus and (d) Hardness versus cube corner indenter penetration depth of oPyrTA films for four different areas.

Figure 9c plots the reduced modulus as a function of indentation depth obtained from indentations performed in two different areas of the **oPyrTA** film. The extrapolation of the linear fit to zero gives values for the reduced modulus of 13.2 and 13.7 ± 0.5 GPa, which are not affected by the substrate. Hardness values versus penetration depth obtained from multiple indentations with the cube corner tip are shown in Figure 9d. The plot shows a spread of results with a U-shape dependence. At low depths (< 100 nm), the hardness increases due to a combination of uncertainties in the indenter area function and surface roughness (Ra ~ 15 nm). At larger depths (> 140 nm), the hardness increases due to the influence of the harder substrate in the measurement. Therefore, the hardness of the **oPyrTA** films was taken at depths of ~ 120 nm, which are free from roughness and substrate effects, with a value of ~ 0.76 ± 0.2 GPa. In order to double-check the modulus and hardness values of the **oPyrTA** films sample, a second method based on continuous stiffness measurements, nanoDMA, was applied (Supporting Information, p.p. S22).[39] The obtained values showed a very good agreement with those obtained from conventional nanoindentation at different loads; the reported hardness and reduced modulus values for the film given in table 1 are an average of both methods, and they confirm the superior stiffness and hardness of the **oPyrTA** films compared to the **oPyrTA** powder embedded in oligomer, with a reduced modulus more than twice the one of the starting oligomer material (see Table 1). We attribute this improvement in properties to closer packing and better alignment of crystalline domains in the nanofilms relative to the composite sample made from **oPyrTA** powder. More importantly, if a similar improvement relative to **oPTA** can be realized in a continuous highly-aligned fibre, it would lead to an unprecedented combination of strength and modulus and thus unrivalled performance against impact. As the first indicators, assuming that hardness is equivalent to strength (σ) and Er to the bulk young's modulus (E), the film has a specific fracture energy of $\sigma^2/2E \approx 14\ J/g$, which is above that of most metals, including steel.

Table 1. . Reduced modulus and hardness calculated by Nanoidentation for **oPTA**, **oPyrTA** and **oPyrTA** nanofilms.

Sample	Er (GPa)	H (GPa)
oPTA	2.8 ± 0.1	0.067 ± 0.006
oPyrTA	5.3 ± 0.1	0.290 ± 0.012
oPyrTA nanofilms	13.4 ± 0.5	0.74 ± 0.2

Conclusions

Substitution of the simple phenyl units of **oPTA** by pyrene groups provides **oPyrTA** as a promising oligomeric structure. FT-IR spectra coupled with DFT calculations indicated stronger intermolecular H-bonding and aromatic π-π stacking interactions in the new oligomer. Splitting of **oPyrTA** macroscale fibres into nanoscale ones, by dissociation of the weaker interfibrous H-bonds by KOH, was manifested by FT-IR spectroscopy, AFM and SEM microscopic techniques. This novel anionic nanoscale building block in DMSO solution, under spatial confinement, and in the presence of a proton source such as water, is gradually neutralized through slow H_2O diffusion into DMSO, providing **oPyrTA** nanofilms. Free-standing **oPyrTA** large nanofilms present a thickness of 50 ± 5 nm, a lateral size of over 180 μm, and a flat texture, manifested by different microscopic techniques. Nanoindentation measurements showed a significant increased elastic modulus and hardness of **oPyrTA** oligomer, compared with commercial **oPTA**. This is dramatically enhanced when **oPyrTA** nanofibers, assemble into a nanofilm under spatial confinement. Work is in progress to perform direct mechanical tests on **oPyrTA** nanofilms and study the orientation of oligomer chains in these improved ensembles.

From a more general point of view, our results show how a combination of molecular design and nanostructuration can lead to novel materials with superior properties.

Conflicts of interest

There are no conflicts to declare.

Acknowledgements

E.M.P. acknowledges funding from the European Union Seventh Framework Program under grant agreement 307609 (ERC-MINT) and the MINECO of Spain (CTQ2014-60541-P and CTQ2017-86060-P) and the Comunidad de Madrid (MAD2D-CM program S2013/MIT-3007); A.R. and B. N.-O. are grateful to MINECO of Spain for grants JdC-2015-26689 and JdC-2015-23531. J.J.V acknowledges financial support from the European Union Seventh Framework Program under grant agreement 678565 (ERC-STEM). The computational work was supported

by the Campus de Excelencia Internacional UAM+CSIC. Additionally, we express our gratitude to the Supercomputing and Bioinnovation Center (SCBI) of the University of Málaga (Spain) for their support and resources. IMDEA Nanociencia acknowledges support from the 'Severo Ochoa' Programme for Centres of Excellence in R&D (MINECO, Grant SEV-2016-0686).

Notes and references

[a] IMDEA Nanoscience, C/Faraday 9, Ciudad Universitaria de Cantoblanco, 28049 Madrid Spain. E-mail: emilio.perez@imdea.org.

[b] IMDEA Materials, Eric Kandel 2, Getafe, 28005 Madrid, Spain. E-mail: juanjose.vilatela@imdea.org.

[c] Departamento de Química Inorgánica, Universidad Complutense de Madrid, 28040, Madrid, Spain.

1. G. Srinivasan and D. H. Reneker, *Polym. Int.*, 1995, **36**, 195-201.
2. Y. Imai, *High Perform. Polym.*, 1995, **7**, 337-345.
3. J. M. García, F. C. García, F. Serna and J. L. de la Peña, *Prog. Polym. Sci.*, 2010, **35**, 623-686.
4. X. Fu, C. Yao and G. Yang, *RSC Advances*, 2015, **5**, 61688-61702.
5. J. A. R. Ruiz, M. Trigo-Lopez, F. C. Garcia and J. M. Garcia, *Polymers*, 2017, **9**, 414-444.
6. Y. Shoji, C. Zhang, T. Higashihara and M. Ueda, *Polym. Chem.*, 2012, **3**, 1978-1981.
7. J. Zhu, W. Cao, M. Yue, Y. Hou, J. Han and M. Yang, *ACS Nano*, 2015, **9**, 2489-2501.
8. L. Zhang, S. Bai, C. Su, Y. Zheng, Y. Qin, C. Xu and Z. L. Wang, *Adv. Funct. Mater.*, 2015, **25**, 5794-5798.
9. J. C. Williams, M. A. B. Meador, L. McCorkle, C. Mueller and N. Wilmoth, *Chem. Mater.*, 2014, **26**, 4163-4171.
10. T. K. Lin, S. J. Wu, J. G. Lai and S. S. Shyu, *Comp. Sci. Technol.*, 2000, **60**, 1873-1878.
11. S. J. Kim, M. H. Cho, D. S. Lim and H. Jang, *Wear*, 2001, **251**, 1484-1491.
12. S. Fidan, A. Palazotto, C. T. Tsai and S. Kumar, *Comp. Sci. Technol.*, 1993, **49**, 291-297.
13. E. G. Chatzi and J. L. Koenig, *Polym.-Plast. Technol. Eng.*, 1987, **26**, 229-270.
14. J. Bae, M. K. Song, Y. J. Park, J. M. Kim, M. Liu and Z. L. Wang, *Angew. Chem., Int. Ed.*, 2011, **50**, 1683-1687.
15. in *Hawley's Condensed Chemical Dictionary*, John Wiley & Sons, Inc., 2007, DOI: 10.1002/9780470114735.hawley09454.
16. D. Tanner, J. A. Fitzgerald and B. R. Phillips, *Angew. Chem. Int. Ed. Engl.*, 1989, **28**, 649-654.
17. I. Azpitarte, A. Zuzuarregui, H. Ablat, L. Ruiz-Rubio, A. Lopez-Ortega, S. D. Elliott and M. Knez, *Chem. Mater.*, 2017, **29**, 10068-10074.
18. M. A. Rabjohns, P. Hodge and P. A. Lovell, *Polymer*, 1997, **38**, 3395-3407.
19. S. Mehdipour-Ataei, Y. Sarrafi and M. Hatami, *Eur. Polym. J.*, 2005, **41**, 2887-2892.
20. M. Takayanagi, T. Kajiyama and T. Katayose, *J. Appl. Polym. Sci.*, 1982, **27**, 3903-3917.
21. R. R. Burch, W. Sweeny, H. W. Schmidt and Y. H. Kim, *Macromolecules*, 1990, **23**, 1065-1072.
22. R. R. Burch and L. E. Manring, *Macromolecules*, 1991, **24**, 1731-1735.
23. M. Yang, K. Cao, L. Sui, Y. Qi, J. Zhu, A. Waas, E. M. Arruda, J. Kieffer, M. D. Thouless and N. A. Kotov, *ACS Nano*, 2011, **5**, 6945-6954.
24. J. Zhu, M. Yang, A. Emre, J. H. Bahng, L. Xu, J. Yeom, B. Yeom, Y. Kim, K. Johnson, P. Green and N. A. Kotov, *Angew. Chem., Int. Ed.*, 2017, **56**, 11744-11748.
25. M. Li, L. Zong, X. Li, J. You, X. Wu, Q. Kong and C. Li, *Carbon*, 2017, **123**, 565-573.
26. Y. Guan, W. Li, Y. Zhang, Z. Shi, J. Tan, F. Wang and Y. Wang, *Comp. Sci. Technol.*, 2017, **144**, 193-201.
27. J. Fan, Z. Shi, L. Zhang, J. Wang and J. Yin, *Nanoscale*, 2012, **4**, 7046-7055.
28. J. F. Rabek, *Polymer photodegradation: mechanisms and experimental methods*, Springer Science & Business Media, 2012.
29. G. Genç, B. Alp, D. Balköse, S. Ülkü and A. Cireli, *J. Appl. Polym. Sci.*, 2006, **102**, 29-38.
30. X. Liu and W. Yu, *J. Appl. Polym. Sci.*, 2005, **99**, 937-944.
31. H. G. Chae and S. Kumar, *J. Appl. Polym. Sci.*, 2006, **100**, 791-802.
32. Note that, although possible, the formation of conformers through 180º rotation around the amide bond is energetically disfavored due to steric clashing between the amide oxygen and the H in positions 4/5 or 9/10 of the pyrene fragment.
33. J. O. Brauckmann, P. Zolfaghari, R. Verhoef, E. A. Klop, G. A. de Wijs and A. P. M. Kentgens, *Macromolecules*, 2016, **49**, 5548-5560.
34. In fact, our model oPTA did not produce nanofilms under identical experimental conditions, most likely due to the characteristic cylindrical fibres of Kevlar.
35. R. Matsuoka, R. Toyoda, R. Shiotsuki, N. Fukui, K. Wada, H. Maeda, R. Sakamoto, S. Sasaki, H. Masunaga, K. Nagashio and H. Nishihara, *ACS Appl. Mater. Interfaces*, 2018, **11**, 2730-2733.
36. R. Matsuoka, R. Sakamoto, K. Hoshiko, S. Sasaki, H. Masunaga, K. Nagashio and H. Nishihara, *J. Am. Chem. Soc.*, 2017, **139**, 3145-3152.
37. W. C. Oliver and G. M. Pharr, *J. Mater. Res.*, 1992, **7**, 1564-1583.
38. *BS EN ISO 14577-4:2007 Metallic materials. Instrumented indentation test for hardness and materials parameters. Test method for metallic and non-metallic coatings*, DOI: 10.3403/30091639.
39. W. C. Oliver and G. M. Pharr, *J. Mater. Res.*, 2004, **19**, 3-20.